Journal of Materials Chemistry A

ROYAL SOCIETY OF CHEMISTRY

PAPER

View Article Online
View Journal | View Issue

Cite this: J. Mater. Chem. A, 2025, 13, 9357

Structurally disordered In_2Te_3 semiconductor: novel insights†

Esteban Zuñiga-Puelles, *[a] Ayberk Özden, [b] Raul Cardoso-Gil, [c] Christoph Hennig, [de] Cameliu Himcinschi, [b] Jens Kortus [b] and Roman Gumeniuk *[a]

Received 6th September 2024
Accepted 10th February 2025

DOI: 10.1039/d4ta06357k

rsc.li/materials-a

The crystal structures of low- (α) and high-temperature (β) modifications of In_2Te_3 are refined for the first time. They crystallize with unique noncentrosymmetric face-centered cubic and half-Heusler arrangements, respectively. Both models are related with each other *via* a *group–subgroup* formalism. The small changes in unit-cell volume and entropy at the α → β structural phase transition indicate that it is of 2nd order. The strong structural disorder in α-In_2Te_3 results in a temperature-dependent behavior of the electrical resistivity similar to that of doped semiconductors (with a well-defined maximum) and extremely low thermal conductivity [$\kappa(T) \leq 0.7$ W m^{-1} K^{-1}]. Additional reasons for the poor electrical and thermal transport are low charge-carrier concentration and mobility, as well as enhanced phonon scattering at point defects, together with the presence of four-phonon processes and a 'rattling' effect. α-In_2Te_3 is found to be an n-type indirect semiconductor with an energy gap of 1.03 eV. All these physical characteristics are intrinsic properties of a high-quality stoichiometric crystal.

1 Introduction

Indium-based semiconductors play one of the central roles in modern electronic technologies. Revealing often direct band gaps and being easily tunable, they have nowadays become prioritized in comparison with widely used and abundant materials, such as silicon and gallium arsenide. Finding applications in the construction of high- (HT) and low-temperature (LT) transistors,[1–8] laser diodes,[9–14] optoelectronics,[15–19] liquid crystal displays,[20–23] *etc.*, they are some of the most sought-after objects for investigations. Among the many such materials, In_2Te_3 attracts special interest due to its potential applications as a catalyst for hydrogen evolution,[24] in photodetectors,[15–19] in gas sensors,[25] as an anode for Li-ion batteries,[26] in photovoltaic power generation,[27–29] and as an alloying component in thermoelectric (TE) generators.[30–35] The development of both latter technologies is of extreme importance with respect to modern attempts in being environmentally friendly. Indeed, In_2Te_3 doped with Se is shown to reveal a band gap suitable for production of single-junction solar cells. Furthermore, it can be used in tandem solar-cell architectures overcoming the ≈33% efficiency limit.[28] Additionally, this chalcogenide finds broad application in TE technology, allowing improvement of the figure-of-merit ($zT \gtrsim 1$) of numerous state-of-the-art materials, *e.g.*, SnTe,[36] GeTe,[37] Bi_2Te_3,[30,31] Sb_2Te_3,[32,33] Ga_2Te_3,[34] InSb,[38] and Cu_2SnSe_4.[35] Recent advances in the development of chalcogen-based TE materials, characterized by ultra-low thermal conductivity due to structural defects with lower dimensionality, are highlighted in ref. 39–47.

Noteworthily, despite being in focus for such important technological uses, the basic knowledge on In_2Te_3 seems to still remain questionable, requiring novel insights. In particular, the structural arrangement and nature of the phase transition are less explored. The available structural models for the low-temperature (LT) α-In_2Te_3 (within space groups $F\bar{4}3m$, $Imm2$ and $I4mm$)[48,49] and high-temperature (HT) β-In_2Te_3 (fcc ZnS prototype)[50] were assumed based on the indexing of powder X-ray diffraction patterns, as well as applying *group–subgroup* crystallographic relations. No structural refinements are known up to now.[51,52] Importantly, quantum mechanical calculations performed assuming all these LT-models resulted in metallic properties for α-In_2Te_3 (material ID: 622511, 1223866 and 1105025),[53] whereas those done for β-In_2Te_3 indicated it to be a semiconductor with a band gap of 1.52 eV.[54] These results are contradictory and suggest that the existing structural models are likely to be incorrect.

[a]Institut für Experimentelle Physik, TU Bergakademie Freiberg, Leipziger Straße 23, 09596 Freiberg, Germany. E-mail: estebanzp1@outlook.com; gumeniuk@physik.tu-freiberg.de

[b]Institut für Theoretische Physik, TU Bergakademie Freiberg, Leipziger Straße 23, 09596 Freiberg, Germany

[c]Max-Planck-Institut für Chemische Physik Fester Stoffe, Nöthnitzer Straße 40, 01187 Dresden, Germany

[d]Helmholtz-Zentrum Dresden-Rossendorf, Institute of Resource Ecology, Bautzner Landstraße 400, 01328 Dresden, Germany

[e]The Rossendorf Beamline at ESRF, CS 40220, 38043 Grenoble Cedex 9, France

† Electronic supplementary information (ESI) available. See DOI: https://doi.org/10.1039/d4ta06357k

The band-gap values obtained for α-In_2Te_3 from different optical spectroscopic measurements vary in the $E_g^{opt} \approx 0.99$–1.22 eV range.[55–61] The nature of the transition (*i.e.*, direct/indirect) remains unclear due to the absence of trustworthy structural data. Studies of the temperature dependencies of the Hall[55,62] and Seebeck[63] coefficients indicated hole- or electron-mediated conduction mechanisms in different samples. These findings agree well with the small homogeneity range reported for α-In_2Te_3.[64–66] However, a relation between the composition and type of conductivity is still less understood. The charge-carrier concentrations at room temperature, of $\approx 10^{10}$ cm^{-3} for p- and $\approx 10^{12}$ cm^{-3} for n-type samples as deduced from Hall-effect measurements, are in line with the observed optical band gaps.[67] Polycrystalline α-In_2Te_3 reveals a low thermal conductivity of 1–1.5 W m^{-1} K^{-1} in a broad temperature range of 300−700 K.[34] However, the underlying physical mechanisms for such an effect have not been elucidated.

In this work, we revisit the structural models of LT and HT polymorphs of In_2Te_3 by using temperature-dependent high-resolution synchrotron X-ray diffraction. To elucidate the nature of the phase transition, determination of the intrinsic physical and thermodynamic properties, and magnetic, electrical and thermal transport measurements combined with optical and spectroscopic analyses were performed. All these characterization studies were carried out on a well-established high-quality stoichiometric In_2Te_3 crystal.

2 Experimental section

2.1 Synthesis

The sample was prepared *via* a solid-state reaction from 5N elemental indium powder and tellurium pieces, cold pressed (5 kN) and mixed in a stoichiometric ratio in an Ar-filled glove-box (MBraun, $p(O_2/H_2O) < 0.1$ ppm). The material mixture was placed inside a quartz tube (length ≈ 10 cm with an inner diameter ≈ 12 cm) and sealed under vacuum (<10^{-5} mbar). The sample was heated in 1 day to 700 C and it was kept at this temperature for 5 hours, then slowly cooled down to 600 C in 5 days and further annealed at this temperature for 5 days. Finally, it was quenched in an ice/water mixture.

2.2 Characterization

Temperature-dependent synchrotron powder X-ray diffraction (PXRD) measurements (λ = 0.61996 Å) were performed at beamline BM20 of the European Synchrotron Radiation Facility (ESRF, Grenoble, France).[68] The sample was manually powdered and sieved to a grain size of ≤20 μm and then enclosed in a quartz-capillary of 0.3 mm inner diameter under an Ar-atmosphere. Phase analysis was carried out with the WinXpow program suite[69] and crystal structure refinements were performed using the WinCSD program package.[70]

A representative sample's surface was analyzed *via* scanning electron microscopy (SEM) and spectroscopic ellipsometry. Local chemical composition and microstructure analyses were carried out using a SEM-JEOL JSM 7800F microscope equipped with a Bruker Quantax 400, XFlash 6||30 (silicon drift detector) EDXS spectrometer. The latter confirmed the sample to be single-phase with a chemical composition of $In_{1.9(1)}Te_{3.1(1)}$ determined from 10 randomly selected points (Fig. S1†).

Differential thermal analysis (DTA) with thermogravimetry (TG) was performed on a bulk piece of ≈20 mg, inspected with an optical microscope. The measurement in the temperature range of 300–1000 K with a heating/cooling rate of 10 K min^{-1} was done using a Netzsch STA 449F3 device.

2.3 Physical properties

Spectroscopic ellipsometry measurements were performed on a polished surface (area >1 cm^2), where the final step was done using 0.25 μm diamond powder. The data was recorded at 50°, 55° and 60° incidence angles in the 0.73–6 eV range using an M2000 J.A. Woollam ellipsometer.

Non-polarized Raman spectra were recorded with a Horiba LABRAM System-HR-800, with a CCD camera, a 600 grooves per mm grating, a HeNe laser (633 nm), and a 50× objective with a N.A. of 0.5 (calibrated with a Si[111]-standard by use of its 520.6 cm^{-1} peak). Neon calibration-lamp spectra were recorded after each measurement to track and correct any shift during the Raman measurements. Temperature-dependent Raman spectra and Raman thermal conductivities were obtained with a Linkam THMS-600 cooling–heating stage. The latter was continuously cooled using a liquid-nitrogen vapor-flow and the samples were fixed with silver paste to the stage.

Low-temperature (LT, $T \leq 300$ K) magnetic susceptibility [$\chi(T)$], specific heat capacity [$c_p(T)$], charge-carrier concentration [$n(T)$] and mobility [$\mu(T)$], electrical resistivity [$\rho(T)$], Seebeck coefficient [$S(T)$] and total thermal conductivity [$\kappa(T)$] measurements were performed with the VSM, HC, VdP-Hall, and TTO modules of a DynaCool-12 from Quantum Design, respectively. The $\chi(T)$ and $c_p(T)$ measurements were performed on sample pieces of ≈19.5 mg and ≈10 mg, respectively.

The Hall-effect measurements using the Van der Pauw four-probe method were performed on a square-shaped plate of ∼5 × 5 × 0.4 mm^3, in contact with platinum wires (25 μm) in a magnetic field of 10 T. Further, $n(T)$ and $\mu(T)$ were calculated from the measurements. High-temperature (HT, 300 K ≤ T ≤ 600 K) $\rho(T)$ and $S(T)$ were measured with an ULVAC ZEM-3 device. Both LT and HT $\rho(T)$, $S(T)$ and $\kappa(T)$ properties were obtained from a bar-shaped sample with dimensions of ∼1.5 × 1.4 × 6.1 mm^3. The HT specific heat was measured on a sample piece of ∼36 mg placed inside an Al_2O_3 crucible using a differential scanning calorimeter, DSC 8500, from PerkinElmer. The heating rate during the measurement was 20 °C min^{-1}.

3 Crystal structure

In order to verify the structural models of low- (LT) and high-temperature (HT) modifications of In_2Te_3, high-resolution (HR) synchrotron PXRD was performed. Selected 2θ-regions of several obtained PXRD patterns, measured at different temperatures, are depicted in Fig. 1. For T < 870 K, all peaks observed therein could be indexed with a unit-cell parameter (UCP) $a \approx 18.5(2)$ Å. Further analysis of the extinction

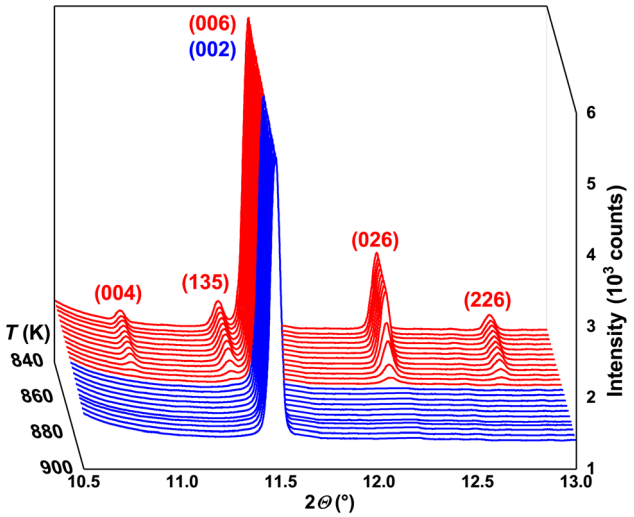

Fig. 1 Selected 2θ-region of synchrotron PXRD patterns for 840 K < T < 900 K together with (*hkl*) indices for LT α- (red) and HT β- (blue) In_2Te_3.

conditions indicated a face-centered cubic lattice with possible space groups (SGs) of $F23$, $Fm\bar{3}$, $F432$, $F\bar{4}3m$ and $Fm\bar{3}m$. This finding prompted us to perform Rietveld refinement assuming the structural model proposed for In_2Te_3.[49,71–73] However, it converged with high reliability factors ($R_I = 0.094$, $R_P = 0.136$) as well as with an atomic thermal displacement parameter (B_{iso}) for the In1-atom in the Wyckoff position 24*f* that is larger by a factor of ≈ 2 than those of all other crystallographic sites. This latter observation would assume partial occupancy for the 24*f* site and thus, a deviation from the experimentally confirmed 2 : 3 stoichiometric composition (Fig. S1†). Being derived by solely applying the *group–subgroup* symmetry reduction to the defective ZnS type, the structural model of α-In_2Te_3 proposed in the literature needs further analysis. Additional proof based on density functional theory (DFT) calculations hinting towards the wrongness of the structural model is provided in ESI.†

Therefore, in the next step we tried to deduce the atomic positions in the studied telluride by applying direct methods. The attempt resulted in the same Te2–Te5 positions as reported earlier (*cf.* Table S2† and data from the ICSD) as well as Te1 at 4*c* and In at 16*e*, 24*g* and 48*h*, which differed from those found in the literature.[49,71–73] Refinement of such a model converged with $R_I = 0.089$, $R_P = 0.134$, the wrong $In_{2.4}Te_3$ composition and the residual electron density (RED) $-2.2/+3.7e$ Å^{-3}. Performed differential Fourier syntheses indicated additional RED at the 4*b* and 24*g* Wyckoff positions. The latter one was already known to be occupied by In-atoms in the model derived from the ZnS type. Having now too much In-concentration in the structure, we refined the site occupancy (G) of the crystallographic sites of these atoms. After this step, the values of the RED were already $-0.71/+0.91e$ Å^{-3}. However, refining the atomic displacement parameters (ADPs), we observed an unphysically large value of B_{iso} for Te1 at the 4*c* position. Shifting it off the center (*i.e.*, assuming this atom to occupy $\approx$ 25% of a 16*e* site with $x = y = z \approx 0.02$), a reliable ADP could be obtained. The final values of the *R*-factors, atomic coordinates, B_{iso} and occupancy obtained from the performed refinement are collected in Tables S1 and S2.† The experimental, theoretical and differential profiles corresponding to these are plotted in Fig. 2 (upper panel). The good agreement of the refined and experimental compositions, together with the improvement of the R_I-factor by almost 30%, indicate the reliability of the obtained model.

Since now the majority of the crystallographic positions shown in Table S2† cannot be derived *via group–subgroup* relation from the ZnS type, the latter model is obviously inconsistent with the HT β-In_2Te_3. However, by performing indexing of the PXRD patterns presented in Fig. S2†, we confirmed the earlier reported UCP $a_{HT} \approx a_{LT}/3 \approx 6.2(1)$ Å as well as the face-centered cubic lattice with the above-mentioned SGs. Keeping in mind that the *klassengleiche* transformation with an index of 9 should work during the $\alpha \rightarrow \beta$ phase transition in In_2Te_3, we attempted direct methods, assuming again the SG $F\bar{4}3m$ for HT-modification. There, two In-atoms are localized at 4*a* and 4*b* and Te at 4*c*. Such a structural arrangement corresponds to the MgAgAs half-Heusler type.[74] It should also be noted that in the prototype compound, the 4*a*-, 4*b*- and 4*c*-sites are occupied by Mg, As and Ag, respectively, which makes the discussion within the *group–subgroup* scheme less conclusive (Fig. S3†). Therefore, in the further considerations we refer to the MnPdTe compound, where Pd and Te are at the 4*b* and 4*c* sites.[75] The *R*-factors of the refinements performed at different temperatures,

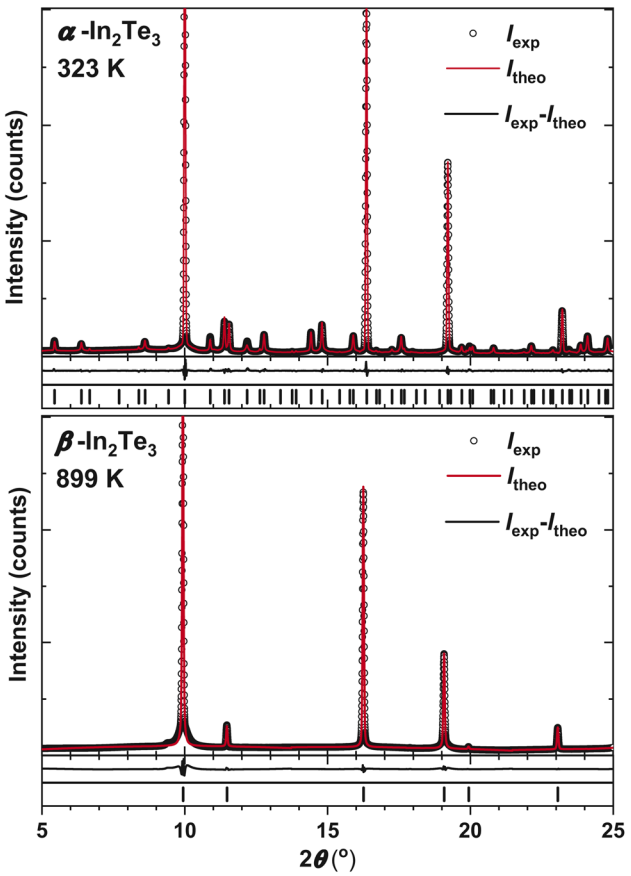

Fig. 2 Synchrotron PXRD patterns and Rietveld refinements for LT α- and HT β-In_2Te_3 together with peak positions, as well as experimental, theoretical and difference profiles.

the obtained atomic coordinates, and the B_{iso} and occupancy values for HT-β-In_2Te_3 are shown in Table S3.† The experimental, theoretical and difference profiles for $T = 323$ K and $T = 899$ K are depicted in Fig. 2.

The shortest interatomic distances in the structures of α- and β-In_2Te_3 are collected in Tables S1 and S3.† Both structures are characterized by no bonding In–In and Te–Te contacts. In contrast, the In–Te distances are shortened by ≈5–12% in comparison with the sum of the covalent radii $r_{(In)} = 1.5$ Å and $r_{(Te)} = 1.37$ Å.[76]

The *group–subgroup* relation scheme between α- and β-In_2Te_3 modifications is presented in Fig. S3.† As expected, the majority of In- and Te-positions in the LT-polymorph are derived from the largely occupied 4*b* and 4*c* sites in the HT-structure. This finding differs from the previously reported model derived from the ZnS type, where both In-positions were deduced from the 4*a* site. In our case, the 24*g* position originating from this site is only ≈17% occupied, in agreement with the low occupancy in the HT-polymorph (*cf.* Tables S2 and S3†). Additionally, the presence of a Te1-atom at 4*c* in the LT-modification would suggest the initial 4*a*-site in β-In_2Te_3 to be occupied with a statistical In/Te mixed site occupancy. However, such a refinement from PXRD data is rather impossible due to the close atomic form factors of indium and tellurium. This problem could be addressed by neutron diffraction on high-quality crystals.[77]

The In1-atom at 4*b* in α-In_2Te_3 can only be derived from the *group–subgroup* scheme if a 4*d* position in the HT-polymorph would be occupied (Fig. S3†). The structure arrangement with the (*dcba*) Wyckoff sequence, SG $F\bar{4}3m$ and $a \approx 6.5(3)$ Å, is known as the $TiCuHg_2$ type.[78] For better visualization, we use in the further discussions its ordered superstructure LiPtMgSb.[79] This structural arrangement is obviously not suitable for β-In_2Te_3, since the 4*d*-site remained non-occupied therein (*i.e.*, the final values of RED after refinement were $-0.14/+0.23e$ Å^{-3}), which raises a question about the correctness of the proposed *group–subgroup* scheme in Fig. S3.† However, accounting for $G = 0.25$ for the In1-atom in the LT-modification, one would expect the 4*d* site occupancy in β-In_2Te_3 to be lower than ≈3%, which is again undetectable within the refinement of the PXRD data. Obviously, as mentioned above, to unambiguously solve the crystal structures of α- and β-In_2Te_3, a temperature-dependent neutron diffraction study is strongly required.

In Fig. 3, the arrangement of polyhedra in the crystal structures of α- and β-In_2Te_3, assuming full occupancies of all crystallographic sites, in comparison with the LiPtMgSb type is presented. As is known, not being a centered structure [*i.e.*, no atom at 4*b* (1/2 1/2 1/2)], ZnS reveals for this site an [□S_4]-tetrahedron, [□Zn_6]-octahedron and [□Zn_8]-cube as the first, second and third coordination spheres, respectively.[80] Centering such a unit cell by adding an atom into the 4*b* Wyckoff position, one would obtain the MgAgAs type (β-In_2Te_3) with an [$In2^{HT}Te_4^{HT}$]-tetrahedron, [$In2^{HT}In1_6^{HT}$]-octahedron and [$In2^{HT}In2_{12}^{HT}$]-cuboctahedron (Fig. S3† and 3b). Adding a further atom at 4*d* (LiPtMgSb type) results in a [$MgPt_4Li_4$]-cube as a first coordination sphere, whereas the second and third ones remain the same as in β-In_2Te_3 (MgAgAs type) (*cf.* Fig. 3a and b). Being

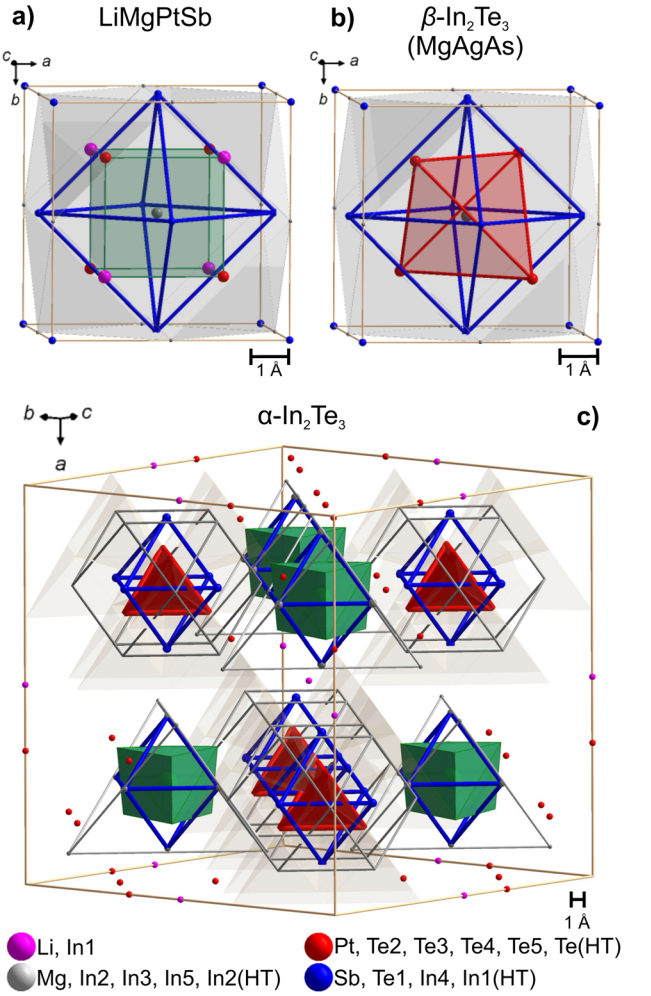

Fig. 3 Structural arrangement and comparison of the LiMgPtSb (a), HT β- (b) and LT α- (c) In_2Te_3 structures.

closely related with both simple prototypes, the α-In_2Te_3 crystal structure reveals a similar arrangement of polyhedra. As one can see from Fig. 3c, there appears an array of corner-sharing [$In5Te4_4$]-tetrahedra (tan) typical for MgAgAs and ZnS types (not shown in Fig. 3a and b). Since the 4*d*-sites are unoccupied in the HT-modification, the [□$Te3_4$]-tetrahedra (red), [□$In4_6$]-octahedra (blue) and [□$In5_{12}$]-cuboctahedra (dark grey) remain empty, in contrast to the MgAgAs prototype. The same observation is made for unoccupied [□$Te1_4Te2_4$]-cubes and [□$In4_6$]-octahedra surrounding them, which resemble the structural units of the LiPtMgSb arrangement. Also, the third coordination sphere of this empty site is only a [□$In2_4$]-tetrahedron (dark grey) (instead of a cuboctahedron, as it is the case for LiPtMgSb), which is due to the unoccupied 16*e* site derived from the 4*b* one (Fig. S3†).

4 Thermal expansion and atomic motion

Selected synchrotron PXRD patterns measured in the 100–974 K temperature range are presented in Fig. 1. All of them reveal

strong and weak intensities (*i.e.*, $I_{strong}/I_{weak} \gtrsim 90$) as well as broadened peak bases. The latter has been attributed to diffuse reflections observed in the diffraction patterns of mechanically sorted single crystals from the same long-term-annealed sample. The diffuse scattering by them hampered any further refinements. Thus, we ascribe the broadening in the PXRD patterns to the intrinsic structural disorder rather than to microstructural effects such as, *e.g.*, stacking faults.

As the temperature increases, some weak reflections become systematically suppressed (*e.g.*, 004, 135, 026 and 226) until they completely disappear at the transition temperature $T_{\alpha\rightarrow\beta} \approx 865$ K (Fig. 1). The strong background increase in the PXRD pattern measured at ~926 K indicates the beginning of the melting process. It becomes completed at $T_{melt} \approx 950$ K as no diffraction peaks are observed. These results agree well with our differential thermal analysis (DTA) (see below) and the reported In–Te phase diagrams ($T_{\alpha\rightarrow\beta}$ and T_{melt} range between 878–915 K and 938–952 K, respectively).[64–66] The small offset between the structurally and thermally determined $T_{\alpha\rightarrow\beta}$ might be attributed to Te-mass losses in the dynamic Ar-flow used during DTA (bulk).

The temperature dependencies of the unit-cell volumes, defined as $a_{LT}{}^3$ and $27a_{HT}{}^3$ for the α and β phases, respectively, are depicted in Fig. 4. The thermal expansion of the LT-modification can be described by a 2nd-order polynomial function in the temperature range of 100–800 K:

$$V^{\alpha}(T) = V_0{}^{\alpha} + V_1{}^{\alpha}T + V_2{}^{\alpha}T^2 \quad (1)$$

with $V_0{}^{\alpha}$, $V_1{}^{\alpha}$ and $V_2{}^{\alpha}$ as fitting parameters (collected in Table 1). The fit is given as a red dotted line in Fig. 4. Hence, the volumetric thermal expansion coefficients are:

$$\alpha_V = \frac{1}{V^{\alpha}(T)}\frac{dV^{\alpha}(T)}{dT} \quad (2)$$

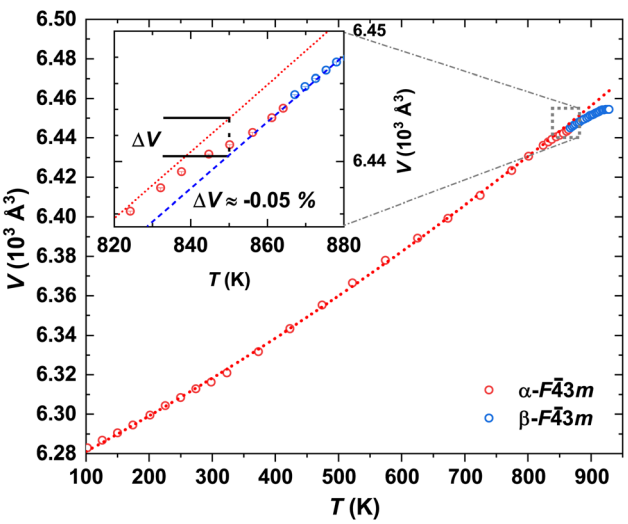

Fig. 4 Temperature-dependent unit-cell volume V of α- and β-In_2Te_3 from 102 K to 974 K together with the fit to eqn (1) (red-dotted line). Inset: Near-phase-transition unit-cell volume variation ΔV estimated at 850 K.

Table 1 Fitting parameters to eqn (1), obtained volumetric thermal expansion coefficient α_V and Grüneisen parameter γ_{XRD} for α-In_2Te_3

Parameters	α-In_2Te_3
Fitted T-range	100–864 K
V_0 (Å^3)	6264(1)
V_1 (Å^3 K^{-1})	0.165(6)
V_2 (Å^3 K^{-2})	5.4(7)× 10^{-5}
α_V (10^{-5} K^{-1})	2.8–4.0
γ_{XRD}	1.5–2.1

As one can see from Table 1 and Fig. S4,† the coefficients are positive and increase with temperature following a classical behavior (Fig. 4). Such a thermal expansion analysis for β-In_2Te_3 is not feasible because it exists in a very narrow T-range (*i.e.*, ≈ 70 K), which is limited by two broad saturation regions in the $27a_{HT}{}^3(T)$ dependence near the structural phase transition (SPT) and the melting point.

Unexpectedly, at $T \approx 820$ K the UCP of α-In_2Te_3 starts to decrease, revealing a weak negative thermal expansion (*i.e.*, reduction of the unit-cell volume $\Delta V \approx -0.05\%$) (Fig. 4 inset). Only after the structural transformation is completed at $T \approx 865$ K (no superstructural peaks are observed) does the UCP start to increase with temperature again. Such a "negative step" in the $a^3(T)$ is in contrast with the behavior of thermal expansion at the SPT (*e.g.*, for the closely related In_2S_3 (ref. 81) as well as with the classical expectations), where a positive jump in this dependence should be the case.[82,83] Nevertheless, an analogous effect has been also observed for TiGePt[84] and $Zn_{2-x}Mg_xP_2O_7$.[85]

Knowing the average speed of sound in α-In_2Te_3 ($v_S = 2560$ ms^{-1})[86] and the Dulong–Petit limit (c_p) we calculate the Grüneisen parameter from the formula $\gamma_{XRD} = \alpha_v v_s{}^2 c_p{}^{-1}$ (Table 1). The obtained value agrees with those observed for many semiconductors (*i.e.*, $\gamma \approx 1$–2)[87] as well as with $\gamma \approx 2.1$ [88] found for the state-of-the-art thermoelectric material SnTe. All these suggest an enhanced phonon anharmonicity.[89]

The temperature dependencies of the isotropic atomic displacement parameters (ADPs) for the α- and β phases are shown in Fig. 5. In agreement with the theory proposed in ref. 90, we observe a small B_{iso} dependence on T, together with their displacements upward by a constant value for the strongly statistically disordered sites (Table. S2†). On the other hand, for atoms at almost fully occupied crystallographic positions, the $B_{iso}(T)$ values for $T > 400$ K are increasing nearly linearly with different slopes, which is a signature of the so-called dynamic disorder.[90] The latter is known to be mainly due to thermal motion of atoms, which can be treated as local vibrations of a quantized harmonic oscillator (Einstein model). Hence, for sufficiently high temperatures (*i.e.*, $h\omega \ll 2k_BT$), $B_{iso}(T)$ is given as:

$$B_{iso}(8\pi)^{-1} = \left(\frac{h^2}{4\pi^2 m_j k_B \Theta_{Ej}{}^2}\right)T \quad (3)$$

where h, k_B, m_j and Θ_{Ej} are the Planck and Boltzmann constants, the reduced mass and the Einstein temperature of the j-atom, respectively.[90,91]

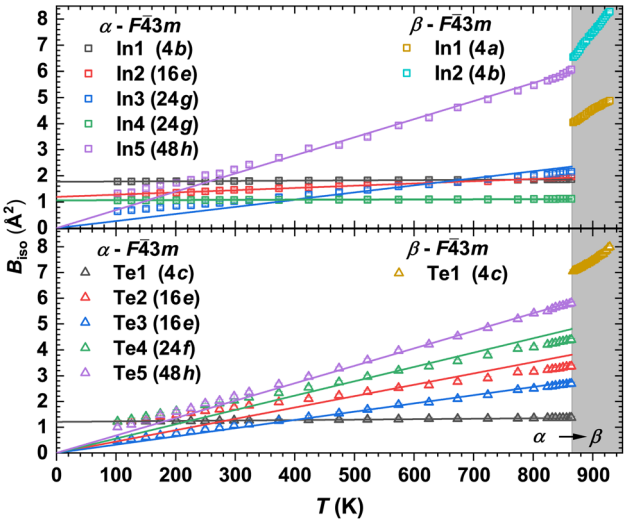

Fig. 5 Temperature dependence of the isotropic atomic displacement parameters (ADPs) in the B_{iso}-representation for both α- and β-In_2Te_3. The ADPs for indium and tellurium atoms are presented in the upper and lower panels, respectively.

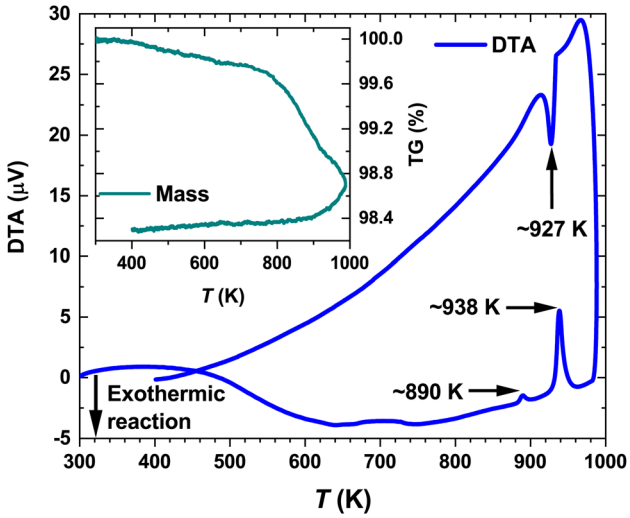

Fig. 6 Temperature dependence of differential thermal analysis (DTA) and thermogravimetry (TG).

Further, applying the definition of a cage-compound[92–94] to α-In_2Te_3, we assume the Te-atoms form an anionic framework incorporating positively charged In-cations. Such a description can be also justified by the larger electronegativity (Pauling scale) of Te ($\chi_{Te} = 2.10$) in comparison to that of indium ($\chi_{In} = 1.78$).[76] This concerns the steepest slope of $B_{iso}(T)$ dependence for In5-atoms, which indicates them to potentially be a 'rattler'.[91] Thus, applying eqn (3), a characteristic $\Theta_E^{In5} = 69(1)$ K (Fig. 5, upper panel) is deduced.

5 Thermodynamics of the phase transition

The temperature-dependent differential thermal analysis and thermogravimetry (DTA-TG) curves of α-In_2Te_3 are presented in Fig. 6. Upon heating, two endothermic peaks corresponding to the α → β phase transition at $T_{α→β} \approx 890$ K and to the melting point at $T_{melt} \approx 938$ K are observed, in agreement with the reported binary In–Te phase diagram.[64–66] On cooling, only the signal at $T_{melt} \approx 927$ K is present, whereas that corresponding to $T_{α→β}$ is not observed. One possible explanation for this effect can be found in the TG curve. As one can see from the Fig. 6 inset, the mass loss is ≈0.4 wt% on heating from 400 K up to 800 K. With a further temperature increase up to 1000 K, it becomes ≈1.5 wt%. This indicates the off-stoichiometry of the studied specimen after heating. Additionally, the PXRD patterns measured in a dynamic Ar-flow revealed the peaks corresponding to the α-modification to be broadened and slightly shifted (to higher 2θ values) due to possible Te-losses.

The temperature dependencies of the specific heat capacity in the $c_pT^{-1}(T)$ representation near the $T_{α→β}$ and T_{melt} transitions are presented in Fig. 7 and the inset therein, respectively. The T_{onset}–T_{offset} ranges of both anomalies agree well with the DTA measurements (Table 2). The discrepancies in the assignment of T_{max} can be explained by the asymmetries of the peaks in the $c_pT^{-1}(T)$ dependencies.

Further, knowing the Dulong–Petit limit $c_p^{DP}T^{-1}$ (see discussion below) and subtracting it as a peak baseline, we calculated the changes in entropy and enthalpy at the $T_{α→β}$ and T_{melt} transitions (Table 2) using $\Delta S = \int c_pT^{-1}dT$ and $\Delta H = \int c_p dT$, respectively. The drastic difference in the obtained $\Delta S(R)$ values (where R is the gas constant) would obviously indicate different orders of the transitions.[83]

To define the α → β structural phase transition in In_2Te_3 as being of 1st order, the following criteria are expected to be fulfilled: (i) the coexistence of both polymorphs at $T_{α→β}$, (ii) a discontinuous change in both unit-cell volume and ΔS, (iii) a sharp symmetric peak in $c_p(T)$ and (iv) $\rho(T)$ hysteresis while performing the measurement in the heating and cooling

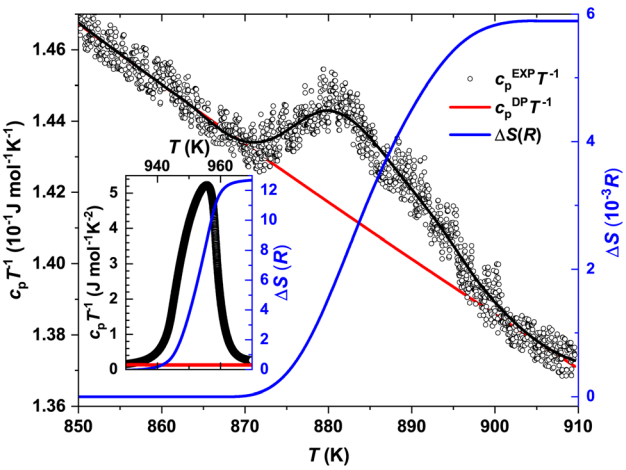

Fig. 7 Specific heat capacity of the α → β phase transition and melting (inset) in the c_pT^{-1} representation (black circles) together with the estimated Dulong–Petit limit (red line) and corresponding entropy calculations (blue line).

Table 2 Entropy ΔS and enthalpy ΔH of the $\alpha \rightarrow \beta$ phase transition and melting for In_2Te_3 together with peak descriptions and comparison to XRD data

	$\alpha \rightarrow \beta$	Melting
$T_{max}^{c_p}$ (K)	882	956
$T_{onset}^{c_p} - T_{offset}^{c_p}$ (K)	865–905	923–970
$T_{\alpha\rightarrow\beta}^{PXRD}$ (K)	865	—
T_{melt}^{PXRD} (K)	—	950
ΔH (J mol^{-1})	~44.6	66× 10^3
ΔS (J mol^{-1} K^{-1})	4.9 × 10^{-2}	~107
$\Delta S(R)$	6 × 10^{-3}	12.9

regimes.[81,82] The first and last criteria from this list have not been proven up to now, whereas points (ii) and (iii), as is clearly visible from the discussions above, are not fulfilled. Obviously, to unambiguously estimate the order of this transition, some additional studies are required.

6 LT specific heat capacity

The specific heat capacity for α-In_2Te_3 in the $c_p/T^3(T)$ representation is depicted in Fig. 8. It reveals a boson peak with a maximum at $T \approx 9$ K originating from the minor and major contributions of low-energy acoustic and optical modes, respectively.[95] However, in the case of a 'rattling' effect, the latter are normally the dominating ones, as has been found for cage compounds.[92–94] In these materials, the low-energy optical phonon modes arise from the low-frequency vibrations of weakly-bonded cations incorporated in the anionic framework. Therefore, for the description of the In_2Te_3 LT specific heat capacity, we applied the combined Debye–Einstein model, given as:

$$c_p(T) = \sum_i C_{Di}(T) + \sum_j C_{Ej}(T) + \gamma T \quad (4)$$

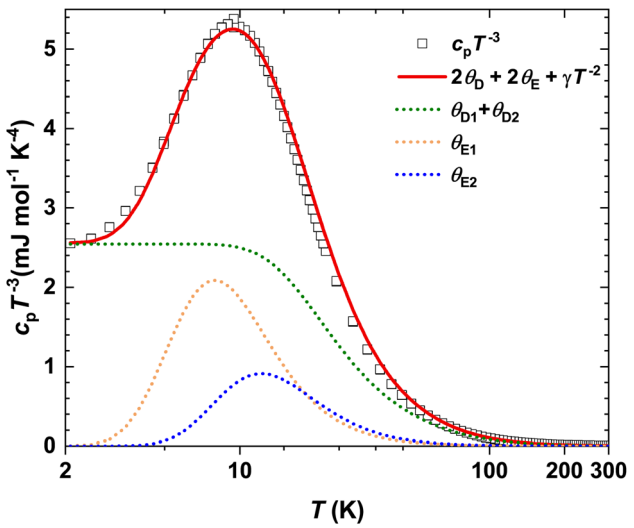

Fig. 8 Temperature dependence of specific heat capacity for α-In_2Te_3 in the c_p/T^3 representation, including the fit (red line) to eqn (4). The individual contributions from eqn (5) and (6) are shown as dotted lines.

with,

$$C_{(Di)}(T) = 3N_{Di}R\left(\frac{T}{\Theta_{Di}}\right)^3 \int_0^{\Theta_{Di}/T} \frac{x^4 e^x}{(e^x-1)^2}\,dx \quad (5)$$

$$C_{Ej}(T) = N_{Ej}R\left(\frac{\Theta_{Ej}}{T}\right)^2 \frac{e^{\Theta_{Ej}/T}}{(e^{\Theta_{Ej}/T}-1)^2} \quad (6)$$

where $C_{Di}(T)$, $C_{Ej}(T)$ and γT stand for the Debye (*i.e.*, strongly bonded framework), Einstein (*i.e.*, vibrational modes of the 'rattler') and electronic contributions, respectively.[96,97]

Since the quantity of Debye terms is defined by the number of elemental constituents in the chemical formula (*i.e.*, two for In_2Te_3) and that of Einstein modes by the amount of 'rattlers', we set $i = 2$ and $j = 1$ in the preliminary model. Further, accounting for the stoichiometric composition of the studied compound, we find the total number of modes to be $N_{tot} = N_{Di} + N_{Ej} = 15$. Knowing from the analysis of the $B_{iso}(T)$ dependencies that only In5 could be a 'rattler' and thus, having 48-fold site symmetry with a site occupancy $G = 0.87$ (Table S2†), one could assume $N_{E1} \approx 3$. Then $N_{Di} = 12$ with $N_{D1} \approx 3$ (for the not-'rattling' In-atom) and $N_{D2} = 9$ (for Te-atoms) should be the case. However, a model based on this concept failed in the description of the peak in the $c_p/T^3(T)$ dependence, which is an indication of a much more complex phonon spectrum of the studied α-In_2Te_3. Such a situation was frequently reported in the literature.[98–101] Therefore, in the next attempt of the fitting we assumed an additional 'rattling' contribution (*i.e.*, $j = 2$), which could originate from the In3-atom due to the observed slope in the $B_{iso}(T)$ dependence. Removing all constrains on all N_{Di} and N_{Ej} values in the fit, the best description is obtained for a model with $N_{D1} = 4(1)$, $N_{D2} = 9(1)$, $N_{E1} = 0.7(1)$, $N_{E2} = 1.1(2)$ and thus $N_{tot} = 14.8$. The corresponding Debye and Einstein temperatures were $\Theta_{D1} = 322(7)$ K, $\Theta_{D2} = 101(5)$ K, $\Theta_{E1} = 39(2)$ K and $\Theta_{E2} = 60(9)$ K, respectively. Such a result indicates an acceptable description of the phonon spectrum of the anionic framework and a model of the 'rattling' motion. Noteworthily, the Θ_{E2} value correlates well with the In5-atom Einstein temperature $\Theta_E^{XRD} = 69(1)$ K deduced from the ADP values, whereas Θ_{E1} is smaller by a factor of ≈3. Obviously, the model given by eqn (4) does not account for the structural disorder and thus, is not providing a complete understanding of the complex phonon spectrum of α-In_2Te_3.

A similar result (*i.e.*, $2\Theta_{E1} \approx \Theta_{E2}$) was obtained for the $Sn_{24}P_{19.4}Br_8$ clathrate (*cf.* Table 1 in the reference), where two 'rattlers' are well established.[102] This would again assume a remarkable difference between the $B_{iso}(T)$ dependencies for those atoms (not reported in ref. 102), which makes less sense in the view of the same physical effect (*i.e.*, thermal motion with enhanced amplitudes within the voids with close volumes). This would bring us to a similar conclusion: the consideration of only the $c_p/T^3(T)$ dependence provides just tentative insights into the 'rattling' problem.

Finally, the negligibly small Sommerfeld coefficient of the electronic specific heat capacity $\gamma = 6.2(9) \times 10^{-8}$ J mol^{-1} K^{-2} is in nice agreement with the semiconducting properties of the studied telluride (*i.e.*, $\gamma = 0$ for no states at the Fermi level),[83]

thus indicating a minor metallic impurity (*cf.* Fig. S5†). The latter is also evidenced by an upturn in the LT diamagnetic susceptibility $\chi(T)$ of α-In_2Te_3 (Fig. S6†).

7 Raman spectroscopy and anharmonic effects

The normalized Raman spectrum for α-In_2Te_3 recorded at RT, together with the peak fitting, is presented in Fig. 9. Our analysis indicates some additional bands compared with earlier data reported for single-crystal,[103] polycrystalline[104] and thin-film[105] samples (Table 3). The observed differences can be mainly attributed to the resolution of the measurement techniques and performed profile descriptions, since no impurities were detected in our specimen *via* chemical, structural or spectroscopic analyses. Obviously, to clarify this issue, some theoretical calculations are strongly required, and these would again become hampered by the strongly disordered crystal structure of α-In_2Te_3.

As is known, both the positions of modes in a Raman spectrum and the thermal expansion of a material are mainly related to the so-called anharmonic effects, which are due to the change in frequencies of lattice vibration with temperature.[106] Therefore, measurement of T-dependent Raman spectra (Fig. 9 inset) allows the elucidation of underlying harmonic and anharmonic phonon processes. For this purpose, the Klemens–Balkanski model is applied. It defines the peak center W and full-width at half-maximum (FWHM) R of the strongest mode as follows:

$$W = W_0 + A_W\left[1 + \frac{2}{e^m - 1}\right] + B_W\left[1 + \frac{3}{e^n - 1} + \frac{3}{(e^n - 1)^2}\right] \quad (7)$$

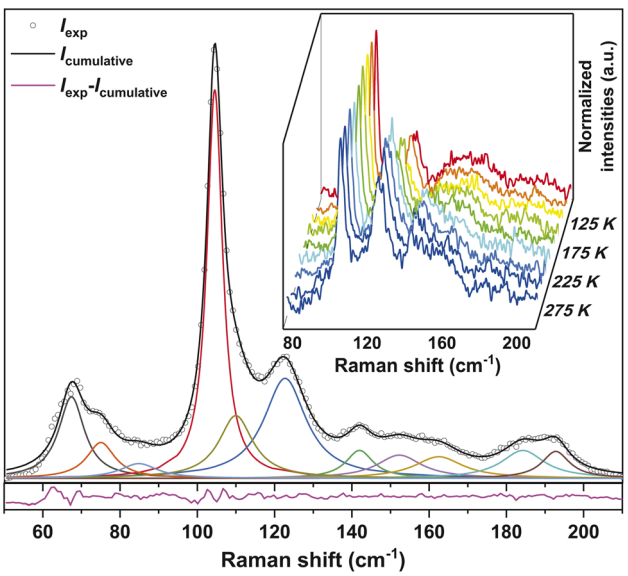

Fig. 9 Normalized α-In_2Te_3 Raman spectrum recorded at 300 K, including refined mode descriptions, cumulative fit and residuals. Inset: Temperature-dependent normalized Raman spectra within the 100–300 K range ($\Delta T = 25$ K).

Table 3 α-In_2Te_3 Raman peak positions (cm^{-1}) in comparison to those reported for single-crystal, polycrystalline and thin-film samples

This work	Single crystal[103]	Polycrystalline[104]	Thin film[105]
67	—	62	—
75	—	73	—
85	—	—	—
104	103	105	—
110	—	—	—
123	125	123	130
142	142	143	—
152/162	157	158	164
184	—	182	—
192	194	194	197

$$R = R_0 + A_R\left[1 + \frac{2}{e^m - 1}\right] + B_R\left[1 + \frac{3}{e^n - 1} + \frac{3}{(e^n - 1)^2}\right] \quad (8)$$

where W_0 and R_0 are the respective projections to 0 K. The coefficients $A_{W,R}$ and $B_{W,R}$ correspond to the three- and four-phonon anharmonic constants, with $m = \hbar W_0/2k_BT$ and $n = \hbar W_0/3k_BT$, respectively.[107] The fits performed accordingly to eqn (7) and (8) are given in Fig. 10 and the inset therein, respectively. The data obtained from them are collected in Table 4.

To describe the $W(T)$ and $R(T)$ behaviors, both $A_{W,R}$ and $B_{W,R}$ contributions were required (Fig. 10). This indicates the presence of both three-phonon (most common in crystalline materials) and four-phonon processes. However, the latter are contributing only $\approx$5% in total. Since W and R in α-In_2Te_3 reveal rather weak T-dependencies, the obtained anharmonic constants are smaller by approximately two-orders of magnitude than those observed for FeS_2 [108] or $PbCuSbS_3$.[98]

8 Spectroscopic ellipsometry

The real (ε_1) and imaginary (ε_2) parts of the dielectric function were calculated (Fig. 11 inset) within a two-phase model (*i.e.*,

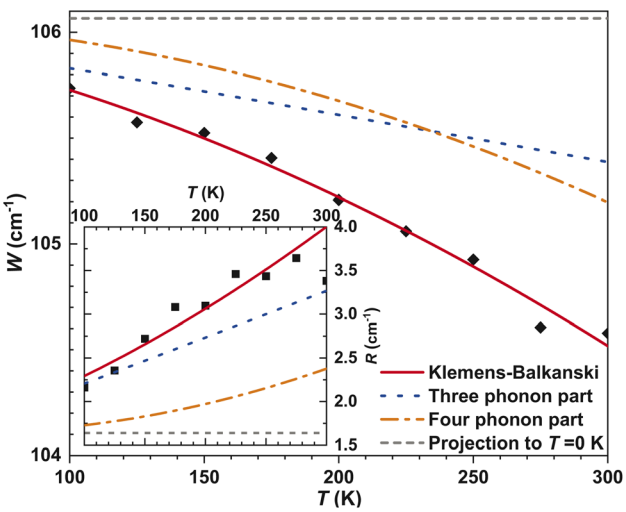

Fig. 10 Klemens–Balkanski analysis of α-In_2Te_3's strongest feature for its peak center and FWHM within the 100–300 K range, including independent contributions to eqn (7) and (8), respectively.

Table 4 Obtained fitting parameters and anharmonic constants for Klemens–Balkanski models eqn (7) and (8), in comparison to FeS_2 and $PbCuSbS_3$

	FeS_2, cm^{-1} (ref. 108)	$PbCuSbS_3$, cm^{-1} (ref. 98)	In_2Te_3, cm^{-1}
W_0	385.26(6)	332.4(3)	106.1(2)
A_W	−1.01(3)	−1.77(30)	−0.09(1)
B_W	—	−0.14(4)	−0.008(1)
R_0	—	—	1.64(5)
A_R	—	—	0.21(4)
W_R	—	—	0.007(5)

air/sample) with a determined surface roughness of 9.5(2) nm. The good quality of the sample (*i.e.*, crystallinity, homogeneity and surface) was evidenced by the respective overlaps of ε_1 and ε_2 for all three incidence angles. The latter was parameterized using five Gaussian oscillators centered at 1.40(1) eV, 2.08(1) eV, 2.66(1) eV, 3.58(1) eV and 4.60(1) eV.

The Tauc plot $[(\alpha E)^{1/2}$ *vs.* $E]$ together with the linear projection to zero absorption is presented in Fig. 11. The s-like shape of the $(\alpha E)^{1/2}$-plot *vs.* the photon energy confirms α-In_2Te_3 to possess an indirect optical band gap with $E_g^{opt} = 1.03(1)$ eV. This value perfectly agrees with the earlier reported one (1.01 eV)[55,56] for a single crystal grown using the Bridgman method. On the other hand, the E_g^{opt} values found for both polycrystalline (1.13 eV)[57] and amorphous (1.22 eV)[58] specimens were slightly larger, which indicates the dependence on the sample microstructure. In this respect, we must again conclude that the crystal studied here is of good quality.

Interestingly, some thin films of α-In_2Te_3 are reported to possess optical gaps of the same magnitude, however with a direct transition.[59–61] Here, we would like to emphasize that in all these works, the estimation of the E_g^{opt} values and their natures was carried out *via* absorption spectroscopy. Importantly, the elipsometric method is much more sensitive in this respect, since it depends only on the polarization changes after interaction with the sample.[109]

9 Electrical transport

9.1 Electrical resistivity and Seebeck coefficient

The temperature dependence of the electrical resistivity $\rho(T)$ for In_2Te_3 is presented in Fig. 12 (left scale). In the LT region, 2–350 K, $\rho(T)$ is varying in a narrow range of ≈ 7.7–8.7×10^{-2} Ω m, revealing a well-defined minimum at $T_{min} \approx 145$ K. With a further temperature increase, the electrical resistivity of In_2Te_3 increases, passes through a maximum centered at $T_{max} \approx 450$ K and then reveals an activation-like decay. Therefore, in the next step, we applied the Arrhenius approximation for the 2–140 K (green line) and 500–800 K (red line) T-ranges to estimate the values of the corresponding band gaps:

$$\rho(T) = \rho_0 \cdot e^{\left(\frac{-E_g^{Arr}}{2k_B T}\right)} \quad (9)$$

Obtained from the fitting parameters were $\rho_0^{LT} = 7.2(1) \times 10^{-2}$ Ω m and $\rho_0^{HT} = 8.2(3) \times 10^{-5}$ Ω m, as well as $E_g^{Arr(LT)} = 0.3(1)$ meV and $E_g^{Arr(HT)} = 0.64(1)$ eV. The latter value is smaller than that determined *via* elipsometric spectroscopy by a factor of $E_g^{opt}/E_g^{Arr} \approx 1.6$.

As is known, the appearance of two energy gaps (E_g) in the $\rho(T)$ dependence is a signature of a doped semiconductor. In this class of materials, the intrinsic E_g is observed in the HT regime, whereas the LT one represents that between the impurity level and the corresponding band edge [*e.g.*, valence band maximum (VBM) or conduction band minimum (CBM)]. In the T-region in-between, the charge-carrier concentration $[n(T)]$ is considered to remain nearly temperature independent, whereas the mobility $[\mu(T)]$ should determine the shape of the $\rho(T)$ curve.[110] Noteworthily, the $E_g^{Arr(LT)}$ value for In_2Te_3 is lower by at least one order of magnitude than those occurring in

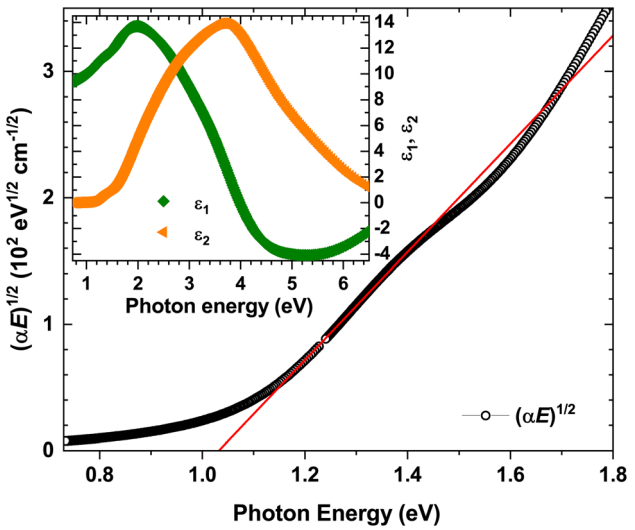

Fig. 11 Tauc plot for indirect optical transitions $[(\alpha E)^{1/2}]$ and band-gap determination by linear projection to zero absorption (red line). Inset: real (ε_1) and imaginary (ε_2) parts of the dielectric function.

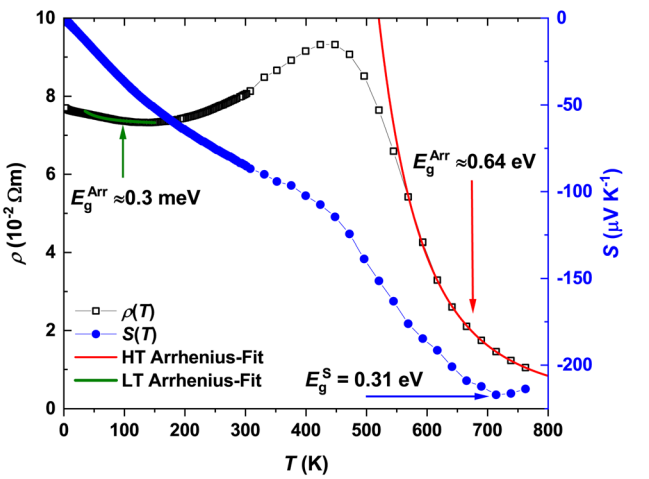

Fig. 12 Temperature dependence of the electrical resistivity $\rho(T)$ and Seebeck coefficent $S(T)$ together with the estimated E_g-values from the Arrhenius approximation (E_g^{Arr}) and Goldsmid–Sharp formula (E_g^S), respectively.

doped semiconductors, as well as being much smaller than $E_g^{Arr(HT)}$.[83] Also, both $n(T)$ and $\mu(T)$ (Fig. 13A and B) are nearly T-independent for 150–250 K and for $T > 270$ K they start to increase and to decrease, respectively. All these observations indicate that despite revealing a $\rho(T)$-shape similar to that of a doped semiconductor, In_2Te_3 cannot be considered as belonging to this class of compounds. Additionally, this finding would be in line with the declared purity of the crystal studied here. Obviously, the observed $\rho(T)$-shape is due to the high number of partially occupied positions in the crystal structure, which possibly can become a source of additional energy levels in close vicinity to the VBM/CBM. Here, we would also like to stress that the origins of such $\rho(T)$ behavior could be of very different natures (*e.g.*, charge density waves,[111,112] topological band structures[113] or simply remaining unclear[114,115]).

The temperature dependence of the Seebeck coefficient $S(T)$ for In_2Te_3 is depicted in Fig. 12 (right scale). $S(T)$ is negative in the whole studied T-range indicating electrons to be the dominant charge carriers. Also, n-type conductivity was earlier reported for the here-studied telluride from Hall effect measurements.[63] However, there are numerous investigations where p-type transport is detected, namely in single crystals[55,56] as well as in thin-films.[59,61] Interestingly, in all these cases, a slight In-excess (*i.e.*, $In_{2+x}Te_3$) was found. The off-stoichiometry of In_2Te_3 would be in line with the In–Te phase diagrams proposed in ref. 64–66.

The Seebeck coefficient of In_2Te_3 decreases with increasing temperature, revealing a well-defined anomaly centered at $T_{kink} \approx 450$ K, coinciding with the maximum in $\rho(T)$. This might be an indication of a switch or change in charge-carrier scattering mechanisms. However, to shed light on such behavior, HT Hall effect measurements would be strongly required. A further temperature increase leads to the appearance of a broad maximum in $|S(T)|$ at $T_{max} \approx 714$ K. Such a behavior of $|S(T)|$ allows the estimation of the energy gap by applying the Goldsmid–Sharp formula:[116]

$$E_g^S = 2e|S_{max}|T_{max} \quad (10)$$

from which $E_g^S = 0.31(1)$ eV is deduced. As expected, this value is different to $E_g^{Arr(HT)}$ and E_g^{opt}. Further, we use the $E_g^S/E_g^{opt} \approx 0.3$ ratio to estimate the majority-to-minority carrier weighted mobility (μ) ratio A:[117]

$$A = \frac{\mu_{maj}}{\mu_{min}}\left(\frac{m^*_{maj}}{m^*_{min}}\right)^{3/2} \quad (11)$$

which is found (following the approaches from Fig. 4 in ref. 117) to be $A \ll 1/50$, which indicates much smaller weighted mobility and thus, explains the large deviation of E_g^S from E_g^{opt}.

9.2 Charge-carrier concentration and mobility

The temperature dependence of α-In_2Te_3's charge-carrier concentration $n(T)$ and mobility $\mu(T)$ are presented in Fig. 13A and B, respectively. They were calculated from the measured Hall coefficients using the $R_H = (en)^{-1}$ and $\mu = (en\rho)^{-1}$ equations, which assume a single band conduction mechanism.[83] Between 100–250 K, $n(T)$ slightly decreases within the range $n \approx 2.45$–2.15×10^{15} cm^{-3} and then it exponentially increases up to $\approx 2.8 \times 10^{15}$ cm^{-3}. In general, the n-magnitude observed here is larger by 3–5 orders of magnitude than those of classical semiconductors ($n \approx 10^{10-12}$ cm^{-3}),[83] and simultaneously smaller by the same factor ($n \approx 10^{18}$ cm^{-3})[118] than the values observed for materials with high thermoelectric (TE) performance. Interestingly, our specimen reveals much larger n at RT in comparison to p- ($n \approx 10^{10}$ cm^{-3})[62] and n-type ($n \approx 10^{12}$ cm^{-3})[67] single crystals studied earlier. The charge-carrier concentration of $\approx 10^{15}$ cm^{-3} could be reached in n-In_2Te_3 only at 556 K.

The values of the charge-carrier mobilities [$\mu(T)$] observed in this work (Fig. 13B) are larger by a factor of $\approx$10 than those previously reported for α-In_2Te_3 at RT (*i.e.*, 32–70 cm^2 V^{-1} s^{-1}).[67] This fact stresses again the strong influence of the structural disorder. Since the $\mu(T)$ decrease for $T \gtrsim 250$ K is compensated by a simultaneous increase in $n(T)$, a smooth variation (rather than a step-like change) is the case in $\rho(T)$ (Fig. 12).

Further, we analyzed the $\mu(T)$-dependence using the $\mu \propto T^m$ power law. Here, m is an indication of different scattering mechanisms.[119,120] Two T-regions were identified within such an approach: (i) $\mu \propto T^{-3/2}$ for 100–250 K and (ii) $\mu \propto T^{-5/2}$ for 250–290 K (red and green lines, respectively, in Fig. 13B). $m = -3/2$ and $m = -5/2$ stand for scattering of charge carriers on only acoustic or on both acoustic and optical phonons, respectively.

To fully understand the scattering mechanisms in α-In_2Te_3, we also analyzed its electrical transport properties within the single parabolic band (SPB) model.[121] The obtained Pisarenko plot confirmed an excellent agreement between the measured $S(n)$ and the theoretically predicted values (Fig. S7†). Also, a fair agreement is observed for the experimental and simulated $\mu(n)$ dependencies for $T > 200$ K (Fig. S8†), hinting towards the dominance of charge-carrier scattering on the acoustic phonons, as discussed above. Finally, this type of analysis indicates the thermoelectric (TE) power factor [$PF(T) = \rho(T)^{-1}S(T)^2T$] for the studied telluride to be close to the maximal

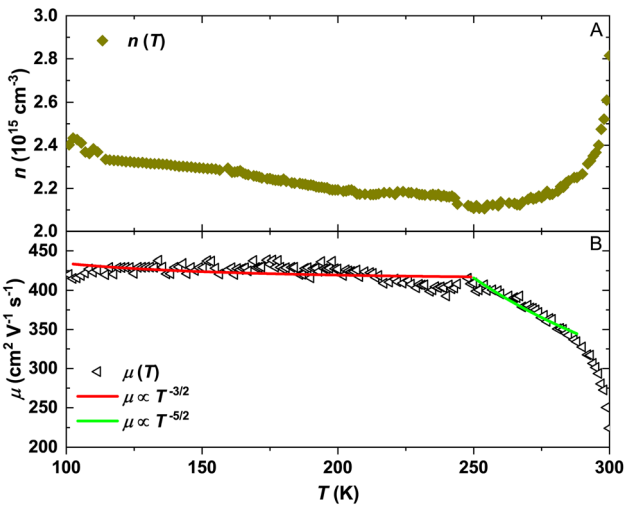

Fig. 13 Temperature dependency of the charge-carrier concentration $n(T)$ (A) and mobility $\mu(T)$ (B) of α-In_2Te_3 assuming a single band conduction mechanism.

expected semiconducting values (Fig. S9†), which means that its drastic increase (*i.e.*, improvement of the TE efficiency) would be possible only while going towards a metallic type of tuning.

Having the hole mobilities $\mu_{min} \approx 210$ and 1380 cm^2 $(V\ s)^{-1}$,[55,56] which were reported for p-type single crystals at RT, together with our value $\mu_{maj} \approx 225$ cm^2 $(V\ s)^{-1}$ (Fig. 13B), we again analyzed eqn (11). Calculating the μ_{maj}/μ_{min}-ratio to be ~46/50 or ~8/50 and assuming $A \approx 1/500$, one can conclude that the effective masses m^*_{min} of holes in α-In_2Te_3 are larger by a factor of 19–60 than those of electrons. The numbers obtained in such a way agree well with the values deduced from theoretical calculations for chemically related In_2S_3 and its doped variant $In_2S_{3-x}Se_x$[122] as well as InSb.[123] All of them also assume the electronic structure of α-In_2Te_3 to be anisotropic and to be characterized by a flat valence band just below the Fermi level E_F, which seems to be in contradiction with the fact that the SPB model fairly describes the electrical transport.[83] Obviously, to shed light on this problem, reasonable DFT simulations would be strongly required, which are still a challenge for state-of-the-art approaches, due to the large unit-cell volume and strong structural disorder in the studied telluride. For more details on this topic, see our discussion on the electronic structure calculation of hypothetically ordered α-In_2Te_3 in the ESI.†

10 Thermal transport

The temperature dependence of the electronic contribution to the thermal conductivity $\kappa_{el}(T)$ is presented in Fig. S10.† It was calculated from the Wiedeman–Franz law: $\kappa_{el} = L(T)T[\rho(T)^{-1}]$, where the Lorenz numbers $L(T)$ (Fig. S10† inset) are obtained from the empirical equation:

$$L(T) = 1.5 + \exp\left(-\frac{|S(T)|}{116}\right) \quad (12)$$

with $|S(T)|$ given in μV K^{-1} and $L(T)$ in 10^{-8} W Ω K^{-2}.[124] As expected, $L(T)$ deviates up to ~30% from its average value because of: i) the different scattering times for electrons and phonons, ii) the larger contribution from phonons and/or iii) the presence of electron inelastic scattering mechanisms.[83] The negligibly small $\kappa_{el}(T) \approx 10^{-3}$ W m^{-1} K^{-1} for $T < 800$ K (Fig. S10†) indicates the thermal transport in In_2Te_3 to be mainly phonon-mediated, which is in good agreement with its semiconducting properties.

The phononic contribution (κ_{ph}) obtained after subtraction of $\kappa_{el}(T)$ from the total thermal conductivity is presented in Fig. 14. It is very low: $\kappa_{ph} \leq 0.7$ W m^{-1} K^{-1} (which is by a factor of ≈2 smaller than that reported for a polycrystalline sample at RT[34]) and thus indicates α-In_2Te_3 to possess potential for possible TE applications.[125] To understand the underlying individual phonon scattering mechanisms, κ_{ph} was further analyzed within the modified Debye–Callaway model:[126]

$$\kappa_{ph} = \frac{{k_B}^4 T^3}{2\pi^2 v_S \hbar^3} \int_0^{\Theta_D/T} \frac{1}{{\tau_{tot}}^{-1}} \frac{x^4 e^x}{(e^x - 1)^2} dx \quad (13)$$

with $x = \hbar\omega/k_BT$, $\Theta_D = 200$ K (obtained from absorption edge measurements[57]) and the total relaxation time ${\tau_{tot}}^{-1}$ depending on three phonon scattering mechanisms as follows:

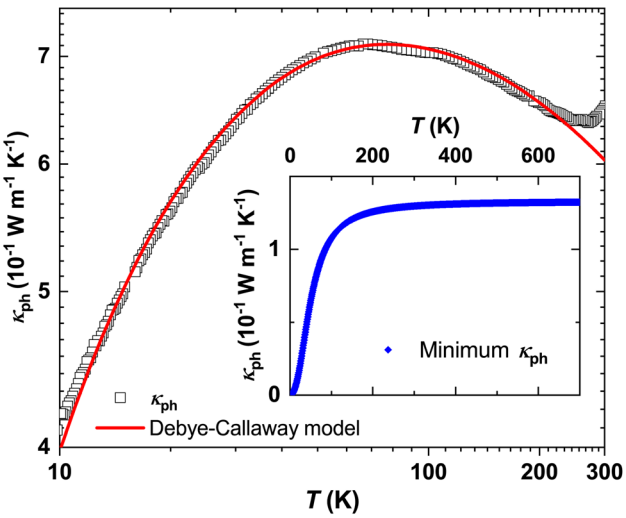

Fig. 14 In_2Te_3 phononic contribution to the thermal conductivity κ_{ph} together with the fit to eqn (13). Inset: Simulated smallest physically achievable κ_{ph} by considering a glass-like state.

$$\tau_{tot}^{-1} = \tau_B^{-1} + \tau_{PD}^{-1} + \tau_U^{-1} \quad (14)$$

where τ_B^{-1}, τ_{PD}^{-1} and τ_U^{-1} stand for the relaxation times of phonon scattering on grain boundaries, point defects and *umklapp* phonon–phonon processes, respectively. In Table 5, the obtained fitting parameters are collected together with the used τ models. As one can see from Fig. 14, we obtain an excellent description of $\kappa_{ph}(T)$ using eqn (13) in the temperature range $T \lesssim 250$ K. The deviations above 250 K are due to the thermal irradiation effects.[127] Interestingly, introducing the normal phonon–phonon processes (τ_N^{-1}) was not necessary to simulate $\kappa_{ph}(T)$, which indicates them to be seemingly screened by the point-defect and *umklapp* scattering mechanisms. Such an effect is theoretically and experimentally discussed for crystal structures with enhanced defect concentrations and/or strong disorder.[39,128]

The τ_B^{-1} value deduced from the fit to eqn (13) indicates a rather large $D = 7650(1)$ Å crystallite size and thus negligibly small phonon scattering on the grain boundaries in the studied telluride. This finding would be in contradiction with the low $\kappa_{ph}(T)$, since large D-values normally imply better conductivity.[129] On the other hand, τ_{PD}^{-1} (calculated using the average volume per atom per unit cell $\bar{V}$) suggests an enlarged point-defect scattering parameter $\Gamma = 1.057(1)$, which should be the case in strongly disordered structures [reported also for $Bi_2Te_{3-x}Se_x$ nanoplates ($\Gamma = 0.18$),[130] nanograined Cu_2Se (Γ =

Table 5 Obtained parameters from individual relaxation-time fits to eqn (14) derived from the Debye–Callaway model eqn (13)

	Model[126]	Fitted parameter
τ_B^{-1}	v_S/D	$D = 7.65(1) \times 10^{-7}$ m
τ_{PD}^{-1}	$\frac{\bar{V}\Gamma}{4\pi {v_S}^3}\left(\frac{k_B}{\hbar}\right)^4 x^4 T^4$	$\Gamma = 1.057(1)$
τ_U^{-1}	$\frac{{\gamma_{th}}^2 {k_B}^2}{M {v_S}^2 \Theta_D \hbar} x^2 T^3 e^{(-\Theta_D/3T)}$	$\gamma_{th} = 2.75(2)$

0.38)[131] and polycrystalline $AgBiSe_2$ ($I = 1.6$)[132]]. Obviously, higher scattering on point defects compensates for the absence of that on grain boundaries in α-In_2Te_3. Finally, in the temperature range $T \gtrsim 100$ K, τ_U^{-1} (calculated using the average atomic mass $\bar{M}$) dominates the thermal transport. From it, we deduce the average thermal Grüneisen parameter $\gamma^{th} = 2.75(2)$ in agreement with γ^{XRD} (Table 1). Our values are similar to those observed for systems [*e.g.*, InTe ($\gamma \approx 3.3$),[133] SnTe ($\gamma \approx 2.1$),[88] In_2Se_3 ($\gamma \approx 5.4$),[134] *etc.*] with high phonon anharmonicity and thus low κ_{ph}.

Assuming disruption of the long-range order in In_2Te_3 (*i.e.*, an amorphous or glass-like state) we calculated the minimal possible phononic thermal conductivity $\kappa_{min}(T)$ of this compound, which is estimated as:

$$\kappa_{min} = \left(\frac{\pi}{6}\right)^{1/3} k_B v_S N^{2/3} \left(\frac{T}{\Theta_i}\right)^2 \int_0^{\Theta_i/T} \frac{x^3 e^x}{(e^x - 1)^2} dx \qquad (15)$$

where N is the number of atoms per unit-cell volume and $\Theta_i = v_s \hbar k_B^{-1} (6\pi^2 N)^{1/3}$.[126,135] As is seen in the Fig. 14 inset, $\kappa_{min}(T)$ saturates with ≈ 0.13 W m^{-1} K^{-1} at $T > 200$ K. This value is close to and in the same order of magnitude as those obtained from the Debye–Callaway model (*i.e.*, ~0.6–0.4 W m^{-1} K^{-1}) at HT. Thus, it confirms κ_{ph} to be intrinsically low and purely related to its disordered and defective crystal structure. Such a scenario is also the case for $Cu_{4-\delta}Ge_3Se_5$, $MnPnS_2Cl$ (Pn = Sb, Bi), $Sn_2SbS_{2-x}Se_xI_3$ and $Sn_2BiS_2I_3$ compounds revealing ultra-low thermal conductivity.[136–138] Using the classical kinetic theory, assuming a diffuse thermal regime and experimental c_p-values, the phonon mean free path for both κ_{ph} and κ_{min} were calculated as $l_{ph} = [3\kappa_{ph}(T)c_p(T)v_s]^{-1}$. This parameter is found to be nearly constant (≈ 1.26 Å for $T > 50$ K) for the amorphous-like state, whereas, for the experimental conditions it was shown to decrease from ≈ 100 Å at 10 K to 5.86 Å at 300 K, respectively. Since in all cases $l_{ph} \ll D$ and in HT regime it is smaller than UCP (Table S2†), the point-defect scattering mechanism and *umklapp* processes (*i.e.*, anharmonicity) are obviously governing the thermal transport in α-In_2Te_3.

Calculating the dimensionless TE figure-of-merit $zT(T) = PF(T)T[\kappa_{ph}(T) + \kappa_{el}(T)]^{-1}$ for In_2Te_3, we found that despite suitable low thermal conductivity, it varies between 10^{-5}–10^{-2}, which is by a few orders of magnitude lower than those observed for state-of-the-art thermoelectric materials.[83] This situation is mainly due to the enhanced electrical resistivity caused by low charge-carrier concentration in this compound.

11 Conclusions

The structural models of the low-temperature (LT) α-In_2Te_3 and high-temperature (HT) β-In_2Te_3 were obtained by applying direct methods to the high-resolution powder synchrotron X-ray diffraction patterns. Both of them revealed new atomic arrangements and their relationship was explained within the *group–subgroup* relations. The small jump in the unit-cell volume together with the lowered entropy may indicate a 2nd order for the α → β structural phase transition.

The temperature dependence of the electrical resistivity of α-In_2Te_3 reveals two regions with an activation-like decay and a well-defined maximum. Since the studied crystal is shown to be of a good quality with no impurities, we ascribe these effects to the high structural disorder and do not classify it as a doped semiconductor. This conclusion is additionally corroborated by the nearly temperature-independent behavior of the charge carriers concentration and their mobility. The Seebeck and Hall coefficients for α-In_2Te_3 are found to be negative in the whole studied T-range, indicating that electrons dominate electrical transport in this material. The analysis performed within the Goldsmid-Sharp approach showed the effective masses of holes to be by a factor of ≈19–60 larger than those of electrons, which assumes the electronic structure of α-In_2Te_3 to be highly anisotropic and to contain flat valence bands.

The T-dependent evolution of the atomic displacement parameter of the In5-atom at the 48*h* crystallographic site, combined with the appearance of a boson peak in the specific heat at low temperatures, indicates a 'rattling' effect in α-In_2Te_3. This is obviously one of the reasons for a very low thermal conductivity ($\kappa_{ph} \leq 0.7$ W m^{-1} K^{-1}) in this compound. Further analysis performed within the Debye–Callaway model has shown extremely strong phonon scattering on point-defects, whereas temperature-dependent Raman spectroscopy indicated the occurrence of four-phonon decay processes. Both effects are again governing the low κ_{ph} and nicely agree with the enhanced values of the Grüneisen parameters deduced from differential thermal (γ^{th}) and structural (γ^{XRD}) analyses. All these findings indicate stronger anharmonicity of phonon processes in α-In_2Te_3. The simulated minimum κ_{ph} dependence confirms that the observed thermal conductivity cannot be significantly reduced by, *e.g.*, nanostructuring, and thus it is an intrinsic effect.

Having a sample of an advanced quality (no transport agents were used for its synthesis), we shed light on the interplay between its strong structural disorder and the underlying electrical and thermal transport mechanisms. Obviously, when redistributing the numerous defects by varying the synthesis conditions of α-In_2Te_3, one can expect some enhancements in charge-carrier density and/or their mobilities, thus improving the electrical transport characteristics. To make such a tuning more predictable, additional theoretical studies concerning electronic and phononic structures are also strongly desired. Undoubtedly, α-In_2Te_3 is a promising system possessing a remarkable potential with respect to its further investigations.

Data availability

The data supporting this article is included as part of the ESI.†

Author contributions

Esteban Zuñiga-Puelles: formal analysis, conceptualization, investigation, methodology, software, validation, visualization, writing – original draft, writing – review & editing. Ayberk Özden: formal analysis, methodology, writing – review & editing. Raul Cardoso-Gil: investigation, writing – review & editing. Christoph Hennig: investigation, writing – review & editing.

Cameliu Himcinschi: funding acquisition, project administration, supervision, writing – review & editing. Jens Kortus: investigation, writing – review & editing. Roman Gumeniuk: funding acquisition, project administration, supervision, validation, visualization, writing – review & editing.

Conflicts of interest

There are no conflicts to declare.

Acknowledgements

This work was performed within the Deutsche Forschungsgemeinschaft (DFG) project 441856638. The DynaCool-12 system was acquired within the DFG Project No. 422219907. The authors thank U. Burkhardt, M. Eckert, S. Kostmann and U. Fischer for metallographic preparation and analyses as well as M. Schmidt and S. Scharsach for the assistance during the DTA/DSC/TG measurements.

Notes and references

1 L. Viscardi, E. Faella, K. Intonti, F. Giubileo, V. Demontis, D. Prete, V. Zannier, L. Sorba, F. Rossella and A. Di Bartolomeo, *Mater. Sci. Semicond. Process.*, 2024, **173**, 108167.
2 P. Dodd, M. Melloch, M. Lundstrom, J. Woodall and D. Pettit, *IEEE Trans. Electron Devices*, 1993, **40**, 2141.
3 Y. Wang, J. Chi, K. Banerjee, D. Grützmacher, T. Schäpers and J. G. Lu, *J. Mater. Chem.*, 2011, **21**, 2459–2462.
4 T. Ashley, M. T. Emeny, D. G. Hayes, K. P. Hilton, R. Jefferies, J. O. Maclean, S. J. Smith, A. W.-H. Tang, D. J. Wallis and P. J. Webber, *2009 IEEE International Electron Devices Meeting (IEDM)*, 2009, pp. 1–4.
5 T. Ashley, A. Dean, C. Elliott, R. Jefferies, F. Khaleque and T. Phillips, *International Electron Devices Meeting. IEDM Technical Digest*, 1997, pp. 751–754.
6 K. J. Bachmann, *Annu. Rev. Mater. Res.*, 1981, **11**, 441–484.
7 J. Ajayan and D. Nirmal, *Superlattices Microstruct.*, 2015, **86**, 1–19.
8 C. Gutsche, A. Lysov, D. Braam, I. Regolin, G. Keller, Z.-A. Li, M. Geller, M. Spasova, W. Prost and F.-J. Tegude, *Adv. Funct. Mater.*, 2012, **22**, 929–936.
9 S. Nakamura, *Semicond. Sci. Technol.*, 1999, **14**, R27.
10 S. Nakamura, M. Senoh, S. ichi Nagahama, N. Iwasa, T. Yamada, T. Matsushita, H. K. H. Kiyoku and Y. S. Y. Sugimoto, *Jpn. J. Appl. Phys.*, 1996, **35**, L74.
11 S. Chichibu, A. Abare, M. Mack, M. Minsky, T. Deguchi, D. Cohen, P. Kozodoy, S. Fleischer, S. Keller, J. Speck, J. Bowers, E. Hu, U. Mishra, L. Coldren, S. DenBaars, K. Wada, T. Sota and S. Nakamura, *Mater. Sci. Eng. B*, 1999, **59**, 298–306.
12 L. J. Stinson, J. G. Yu, S. D. Lester, M. J. Peanasky and K. Park, *Appl. Phys. Lett.*, 1991, **58**, 2012–2014.
13 H. Tanaka, Y. Kawamura, S. Nojima, K. Wakita and H. Asahi, *J. Appl. Phys.*, 1987, **61**, 1713–1719.
14 S. Sassen, B. Witzigmann, C. Wolk and H. Brugger, *IEEE Trans. Electron Devices*, 2000, **47**, 24–32.
15 Z. Yang, J. Guo, H. Li, X. Du, Y. Zhao, H. Chen, W. Chen and Y. Zhang, *Mater. Des.*, 2023, **233**, 112218.
16 Z. Wang, M. Safdar, C. Jiang and J. He, *Nano Lett.*, 2012, **12**, 4715–4721.
17 J. Yao, Z. Deng, Z. Zheng and G. Yang, *ACS Appl. Mater. Interfaces*, 2016, **8**, 20872–20879.
18 Z. M. Grushka, P. N. Gorley, O. G. Grushka, P. P. Horley, Y. I. Radevych and Z. Zhuo, *ICO20: Materials and Nanostructures*, 2006, p. 60291A.
19 X. Zhang, W. Sun, Z. Lu, L. Zhang, L. Zhao, J. Ding and G. Yan, *Infrared Materials, Devices, and Applications*, 2008, p. 68350A.
20 J. F. Algorri, N. Bennis, V. U. del Pozo, P. Morawiak, L. R. Jaroszewicz and J. M. S. Pena, *Novel Optical Systems, Methods, and Applications XXII*, 2019, p. 1110510.
21 P. Yeh and C. Gu, *Optics of Liquid Crystal Displays*, John Wiley & Sons, 2009, vol. 67.
22 R. S. Datta, N. Syed, A. Zavabeti, A. Jannat, M. Mohiuddin, M. Rokunuzzaman, B. Yue Zhang, M. A. Rahman, P. Atkin, K. A. Messalea, et al., *Nat. Electron.*, 2020, **3**, 51–58.
23 Z. Liu, C.-Y. Huang, H. Liu, X. Zhang and C. Lee, *Opt. Express*, 2013, **21**, 6519–6525.
24 X. Yang, A. Banerjee, Z. Xu, Z. Wang and R. Ahuja, *J. Mater. Chem. A*, 2019, **7**, 27441–27449.
25 R. Desai, D. Lakshminarayana, P. Patel and C. Panchal, *Sens. Actuators, B*, 2005, **107**, 523–527.
26 S. So, J. Ko, Y. N. Ahn, I. T. Kim and J. Hur, *Chem. Eng. J.*, 2022, **429**, 132395.
27 A. A. Zahab, M. Abd-Lefdil and M. Cadene, *Phys. Status Solidi A*, 1990, **119**, K35–K39.
28 W. Li, X.-F. Cai, N. Valdes, T. Wang, W. Shafarman, S.-H. Wei and A. Janotti, *J. Phys. Chem. Lett.*, 2022, **13**, 12026–12031.
29 M. H. Ali, M. A. Al Mamun, M. D. Haque, M. F. Rahman, M. K. Hossain and A. Z. Md. Touhidul Islam, *ACS Omega*, 2023, **8**, 7017–7029.
30 D. Liu, X. Li, P. M. d. C. Borlido, S. Botti, R. Schmechel and M. Rettenmayr, *Sci. Rep.*, 2017, **7**, 43611.
31 D. Liu, J. Stötzel, M. Seyring, M. Drüe, X. Li, R. Schmechel and M. Rettenmayr, *Cryst. Growth Des.*, 2016, **16**, 617–624.
32 S. Vallem, K. V. Bangera and S. G. K., *Superlattices Microstruct.*, 2019, **131**, 15–20.
33 A. Rosenberg and A. Strauss, *J. Phys. Chem. Solids*, 1961, **19**, 105–116.
34 S. Yamanaka, M. Ishimaru, A. Charoenphakdee, H. Matsumoto and K. Kurosaki, *J. Electron. Mater.*, 2009, **38**, 1392–1396.
35 L. Qu, C. Yang, Y. Luo, Z. Du, C. Li and J. Cui, *ACS Appl. Mater. Interfaces*, 2022, **14**, 45628–45635.
36 G. Tan, W. G. Zeier, F. Shi, P. Wang, G. J. Snyder, V. P. Dravid and M. G. Kanatzidis, *Chem. Mater.*, 2015, **27**, 7801–7811.
37 H. Sun, X. Lu, H. Chi, D. T. Morelli and C. Uher, *Phys. Chem. Chem. Phys.*, 2014, **16**, 15570–15575.
38 Y. Pei and D. T. Morelli, *Appl. Phys. Lett.*, 2009, **94**, 122112.
39 R. Hanus, R. Gurunathan, L. Lindsay, M. T. Agne, J. Shi, S. Graham and G. Jeffrey Snyder, *Appl. Phys. Rev.*, 2021, **8**, 031311.

40 E. S. Toberer, L. L. Baranowski and C. Dames, *Annu. Rev. Mater. Res.*, 2012, **42**, 179–209.
41 J. He and T. M. Tritt, *Science*, 2017, **357**, eaak9997.
42 A. El Sachat, F. Alzina, C. M. Sotomayor Torres and E. Chavez-Angel, *Nanomater.*, 2021, **11**, 175.
43 T. Ghosh, M. Dutta, D. Sarkar and K. Biswas, *J. Am. Chem. Soc.*, 2022, **144**, 10099–10118.
44 Y. Zheng, T. J. Slade, L. Hu, X. Y. Tan, Y. Luo, Z.-Z. Luo, J. Xu, Q. Yan and M. G. Kanatzidis, *Chem. Soc. Rev.*, 2021, **50**, 9022–9054.
45 H. Han, L. Zhao, X. Wu, B. Zuo, S. Bian, T. Li, X. Liu, Y. Jiang, C. Chen, J. Bi, J. Xu and L. Yu, *J. Mater. Chem. A*, 2024, **12**, 24041–24083.
46 C.-D. Zhou, B. Liang, W.-J. Huang, J.-G. Noudem, X.-J. Tan and J. Jiang, *Rare Met.*, 2023, **42**, 2825–2839.
47 P. Baskaran and M. Rajasekar, *RSC Adv.*, 2024, **14**, 21706–21744.
48 T. Karakostas and N. A. Economou, *Phys. Status Solidi A*, 1975, **31**, 89–99.
49 J. Woolley, B. Pamplin and P. Holmes, *J. Less Common. Met.*, 1959, **1**, 362–376.
50 H. Hahn, W. Klingler and Z. Anorg, *Chem*, 1949, **260**, 97–109.
51 D. Zagorac, H. Müller, S. Ruehl, J. Zagorac and S. Rehme, *J. Appl. Crystallogr.*, 2019, **52**, 918–925.
52 S. Gražulis, A. Daškevič, A. Merkys, D. Chateigner, L. Lutterotti, M. Quirós, N. R. Serebryanaya, P. Moeck, R. T. Downs and A. Le Bail, *Nucleic Acids Res.*, 2012, **40**, D420–D427.
53 A. Jain, S. P. Ong, G. Hautier, W. Chen, W. D. Richards, S. Dacek, S. Cholia, D. Gunter, D. Skinner, G. Ceder and K. A. Persson, *APL Mater.*, 2013, **1**, 011002.
54 A. Vora-ud, C. Thanachayanont, S. Jugsujinda, V. Amornkitbamrung and T. Seetawana, *Procedia Eng.*, 2011, **8**, 2–7.
55 S. Sen and D. Bose, *Solid State Commun.*, 1984, **50**, 39–42.
56 A. T. Nagat, M. M. Nassary and H. A. El-Shaikh, *Semicond. Sci. Technol.*, 1991, **6**, 979–982.
57 O. H. Hughes, P. M. Nikolić, C. J. Doran and S. S. Vujatović, *Phys. Status Solidi B*, 1975, **71**, 105–109.
58 S. Ozaki, K. T. K. Takada and S. A. S. Adachi, *Jpn. J. Appl. Phys.*, 1994, **33**, 6213–6217.
59 R. Desai, D. Lakshminarayana, P. Patel and C. Panchal, *J. Mater. Sci.*, 2006, **41**, 2019–2023.
60 R. Rousina and G. Yousefi, *Mater. Lett.*, 1990, **9**, 263–265.
61 V. Sowjanya, K. V. Bangera and G. Shivakumar, *Ceram. Int.*, 2017, **43**, 3748–3751.
62 S. A. Hussein and A. T. Nagat, *Phys. Status Solidi A*, 1989, **114**, K205–K209.
63 V. P. Zhuse, V. M. Sergeeva and A. I. Shelykh, *Sov. Phys. Solid State*, 1961, **2**, 2545–2555.
64 T. B. Massalski and H. Okamoto, *Binary Alloy Phase Diagrams*, ASM International, 2nd edn, 1990.
65 C.-S. Oh and D. N. Lee, *Calphad*, 1993, **17**, 175–187.
66 V. Zlomanov, M. Sheiman and B. Legendre, *J. Phase Equilib.*, 2001, **22**, 339–344.
67 In_2Te_3 transport properties: Datasheet from Landolt-Börnstein – Group III Condensed Matter Volume 41E: Ternary Compounds, Organic Semiconductors in SpringerMaterials, Copyright 2000 Springer-Verlag Berlin Heidelberg.
68 A. C. Scheinost, J. Claussner, J. Exner, M. Feig, S. Findeisen, C. Hennig, K. O. Kvashnina, D. Naudet, D. Prieur, A. Rossberg, M. Schmidt, C. Qiu, P. Colomp, C. Cohen, E. Dettona, V. Dyadkin and T. Stumpf, *J. Synchrotron Radiat.*, 2021, **28**, 333–349.
69 *STOE Powder Software, WinXPow (Version 2), Darmstadt, STOE and Cie*. GmbH, 2001.
70 L. Akselrud and Y. Grin, *J. Appl. Crystallogr.*, 2014, **47**, 803–805.
71 S. Sugaike and J. Miner, *Pet. Sci.*, 1957, **2**, 63–77.
72 A. Kunjomana and E. Mathai, *Mater. Res. Bull.*, 1991, **26**, 1347–1353.
73 V. Zhuze, A. Zaslavskii, V. Petrusevich, et al., *Proc. Int. Conf. Phys. Semicond.*, 1960, 871–881.
74 H. Nowotny and W. Sibert, *Int. J. Mater. Res.*, 1941, **33**, 391–394.
75 R. Helmholdt and K. Buschow, *J. Less-Common Met.*, 1986, **123**, 169–173.
76 J. Emsley, *The Elements*: Oxford University Press, 1998.
77 T. Schröder, T. Rosenthal, S. Grott, C. Stiewe, J. de Boor and O. Oeckler, *Z. Anorg. Allg. Chem.*, 2013, **639**, 2536–2541.
78 M. Pušelj and Z. Ban, *Croat. Chem. Acta*, 1969, **41**, 79–83.
79 J. Drews, U. Eberz and H.-U. Schuster, *J. Less Common. Met.*, 1986, **116**, 271–278.
80 M. O'Keeffe and B. G. Hyde, *Crystal Structures, Patterns and Symetry*, Courier Dover Publications, 2020.
81 P. Wyżga, W. Carrillo-Cabrera, L. Akselrud, I. Veremchuk, J. Wagler, C. Hennig, A. A. Tsirlin, A. Leithe-Jasper, E. Kroke and R. Gumeniuk, *Dalton Trans.*, 2020, **49**, 15903–15913.
82 U. Müller, *Symmetry Relationships between Crystal Structures: Applications of Crystallographic Group Theory in Crystal Chemistry*, Oxford University Press, 2013.
83 R. Gross, A. Marx, D. Einzel and S. Geprägs, *Festkörperphysik: Aufgaben und Lösungen*, De Gruyter, 2018.
84 S.-V. Ackerbauer, A. Senyshyn, H. Borrmann, U. Burkhardt, A. Ormeci, H. Rosner, W. Schnelle, M. Gamża, R. Gumeniuk, R. Ramlau, E. Bischoff, J. C. Schuster, F. Weitzer, A. Leithe-Jasper, L. H. Tjeng and Y. Grin, *Chem. Eur J.*, 2012, **18**, 6272–6283.
85 Y. Kadowaki, R. Kasugai, Y. Yokoyama, N. Katayama, Y. Okamoto and K. Takenaka, *Appl. Phys. Lett.*, 2021, **119**, 201906.
86 In_2Te_3 sound velocity, refractive index, dielectric constant: Datasheet from Landolt–Börnstein – Group III Condensed Matter Volume 41E: Ternary Compounds,Organic Semiconductors in SpringerMaterials.
87 C. Chang and L.-D. Zhao, *Mater. Today Phys.*, 2018, **4**, 50–57.
88 T. F. Smith, J. A. Birch and J. G. Collins, *J. Phys. C: Solid State Phys.*, 1976, **9**, 4375–4382.
89 G. A. Slack, *J. Phys. Chem. Solids*, 1973, **34**, 321–335.
90 J. D. Dunitz, V. Schomaker and K. N. Trueblood, *J. Phys. Chem.*, 1988, **92**, 856–867.
91 B. C. Sales, B. C. Chakoumakos, D. Mandrus and J. W. Sharp, *18th International Conference on*

Thermoelectrics. Proceedings, ICT'99 (Cat. No. 99TH8407), 1999, pp. 525–530.
92 G. S. Nolas, *The Physics and Chemistry of Inorganic Clathrates*, Springer Netherlands, 2014.
93 C. Uher, in *Recent Trends in Thermoelectric Materials Research I*, ed. T. M. Tritt, Elsevier, 2001, vol. 69 of Semiconductors and Semimetals, pp. 139–253.
94 R. Gumeniuk, *Handbook on the Physics and Chemistry of Rare Earths*, Elsevier, 2018, 54, pp. 43–143.
95 M. Baggioli and A. Zaccone, *J. Mater. Phys.*, 2020, **3**, 015004.
96 M. Beekman, W. Schnelle, H. Borrmann, M. Baitinger, Y. Grin and G. S. Nolas, *Phys. Rev. Lett.*, 2010, **104**, 018301.
97 Y. Ikeuchi, H. Takatsu, C. Tassel, C. M. Brown, T. Murakami, Y. Matsumoto, Y. Okamoto and H. Kageyama, *Inorg. Chem.*, 2019, **58**, 6790–6795.
98 E. Zuñiga-Puelles, R. Cardoso-Gil, A. Özden, N. Bulut, V. Svitlyk, C. Himcinschi, J. Kortus and R. Gumeniuk, *Phys. Rev. B*, 2022, **106**, 195201.
99 E. Zuñiga-Puelles, A. Özden, V. Pacheco, L. Akselrud, R. Cardoso-Gil, A. Straßheim, P. Wyżga, C. Himcinschi and R. Gumeniuk, *J. Alloys Compd.*, 2024, **976**, 173055.
100 W. Schnelle, A. Leithe-Jasper, H. Rosner, R. Cardoso-Gil, R. Gumeniuk, D. Trots, J. A. Mydosh and Y. Grin, *Phys. Rev. B:Condens. Matter Mater. Phys.*, 2008, **77**, 094421.
101 R. Gumeniuk, V. Levytskyi, B. Kundys and A. Leithe-Jasper, *Phys. Rev. B*, 2023, **108**, 214515.
102 V. V. Novikov, A. V. Matovnikov, N. V. Mitroshenkov, B. I. Kornev, K. S. Pilipenko, M. S. Likhanov and A. V. Shevelkov, *Dalton Trans.*, 2017, **46**, 9110–9117.
103 T. D. Golding, P. R. Boyd, M. Martinka, P. M. Amirtharaj, J. H. Dinan, S. B. Qadri, D. R. T. Zahn and C. R. Whitehouse, *J. Appl. Phys.*, 1989, **65**, 1936–1941.
104 E. Finkman, J. Tauc, R. Kershaw and A. Wold, *Phys. Rev. B:Condens. Matter Mater. Phys.*, 1975, **11**, 3785–3794.
105 M. Emziane, J. Bernède, J. Ouerfelli, H. Essaidi and A. Barreau, *Mater. Chem. Phys.*, 1999, **61**, 229–236.
106 X. Gong, H. Wu, D. Yang, B. Zhang, K. Peng, H. Zou, L. Guo, X. Lu, Y. Chai, G. Wang and X. Zhou, *Vib. Spectrosc.*, 2020, **107**, 103034.
107 M. Balkanski, R. F. Wallis and E. Haro, *Phys. Rev. B:Condens. Matter Mater. Phys.*, 1983, **28**, 1928.
108 A. Özden, E. Zuñiga-Puelles, J. Kortus, R. Gumeniuk and C. Himcinschi, J. Raman Spectr., 2023, **54**, 84–92.
109 *Spectroscopic Ellipsometry for Photovoltaics. Volume 1: Fundamental Principles and Solar Cell Characterization*, ed. H. Fujiwara and R. W. Collins, Springer, Cham, 2019.
110 R. E. Hummel, *Electronic Properties of Materials*, Springer Berlin Heidelberg, 2001.
111 L. Krasavin, A. Titov and V. Antropov, *Phys. Solid State*, 1998, **40**, 1962–1964.
112 N. Selezneva, E. Sherokalova, V. Pleshchev, V. Kazantsev and N. Baranov, *J. Phys.: Condens. Matter*, 2016, **28**, 315401.
113 D. Wu, Y. Qian, Z. Liu, W. Wu, Y. Li, S. Na, Y. Shao, P. Zheng, G. Li, J. Cheng, H. Weng and J. Luo, *Chin. Phys. B*, 2020, **29**, 037101.
114 R. Gumeniuk, L. Akselrud, K. O. Kvashnina, W. Schnelle, A. A. Tsirlin, C. Curfs, H. Rosner, M. Schöneich, U. Burkhardt, U. Schwarz, Y. Grin and A. Leithe-Jasper, *Dalton Trans.*, 2012, **41**, 6299–6309.
115 S. Flipo, H. Rosner, M. Bobnar, K. O. Kvashnina, A. Leithe-Jasper and R. Gumeniuk, *Phys. Rev. B*, 2021, **103**, 195121.
116 H. J. Goldsmid and J. W. Sharp, *J. Electron. Mater.*, 1999, **28**, 869–872.
117 Z. M. Gibbs, H.-S. Kim, H. Wang and G. J. Snyder, *Appl. Phys. Lett.*, 2015, **106**, 022112.
118 M. Wolf, R. Hinterding and A. Feldhoff, *Entropy*, 2019, **21**, 1058.
119 C. Herring, *Phys. Rev.*, 1954, **96**, 1163.
120 S. S. Li, in *Scattering Mechanisms and Carrier Mobilities in Semiconductors*, Springer New York, 2006, pp. 211–244.
121 J. Zhu, X. Zhang, M. Guo, J. Li, J. Hu, S. Cai, W. Cai, Y. Zhang and J. Sui, *npj Comput. Mater.*, 2021, **7**, 116.
122 P. Wyżga, S. Grimm, V. Garbe, E. Zuñiga-Puelles, C. Himcinschi, I. Veremchuk, A. Leithe-Jasper and R. Gumeniuk, *J. Mater. Chem. C*, 2021, **9**, 4008–4019.
123 Y.-S. Kim, K. Hummer and G. Kresse, *Phys. Rev. B:Condens. Matter Mater. Phys.*, 2009, **80**, 035203.
124 H.-S. Kim, Z. M. Gibbs, Y. Tang, H. Wang and G. J. Snyder, *APL Mater.*, 2015, **3**, 041506.
125 G. J. Snyder, in *Thermoelectric Energy Harvesting*, ed. S. Priya and D. J. Inman, Springer US, Boston, MA, 2009, pp. 325–336.
126 T. M. Tritt, *Thermal Conductivity: Theory, Properties, and Applications*, Springer New York, NY, 2005.
127 K. A. Borup, J. De Boor, H. Wang, F. Drymiotis, F. Gascoin, X. Shi, L. Chen, M. I. Fedorov, E. Müller, B. B. Iversena, et al., *Energy Environ. Sci.*, 2015, **8**, 423–435.
128 A. A. Maznev and O. B. Wright, *Am. J. Phys.*, 2014, **82**, 1062–1066.
129 E. Zuñiga-Puelles, R. Cardoso-Gil, M. Bobnar, I. Veremchuk, C. Himcinschi, C. Hennig, J. Kortus, G. Heide and R. Gumeniuk, *Dalton Trans.*, 2019, **48**, 10703–10713.
130 M. Hong, T. C. Chasapis, Z.-G. Chen, L. Yang, M. G. Kanatzidis, G. J. Snyder and J. Zou, *ACS Nano*, 2016, **10**, 4719–4727.
131 J. Chen, T. Liu, D. Bao, B. Zhang, G. Han, C. Liu, J. Tang, D. Zhou, L. Yang and Z.-G. Chen, *Nanoscale*, 2020, **12**, 20536–20542.
132 F. Böcher, S. P. Culver, J. Peilstöcker, K. S. Weldert and W. G. Zeier, *Dalton Trans.*, 2017, **46**, 3906–3914.
133 M. K. Jana, K. Pal, U. V. Waghmare and K. Biswas, *Angew. Chem. Int. Ed.*, 2016, **55**, 7792–7796.
134 F. Guo, Y. Lyu, M. B. Jedrzejczyk, Y. Zhao, W. F. Io, G. Bai, W. Wu and J. Hao, *Appl. Phys. Lett.*, 2020, **116**, 113101.
135 D. G. Cahill and R. Pohl, *Solid State Commun.*, 1989, **70**, 927–930.
136 B. Shan, S. Lin, Z. Bu, J. Tang, Z. Chen, X. Zhang, W. Li and Y. Pei, *J. Mater. Chem. A*, 2020, **8**, 3431–3437.
137 N. Sato, N. Kuroda, S. Nakamura, Y. Katsura, I. Kanazawa, K. Kimura and T. Mori, *J. Mater. Chem. A*, 2021, **9**, 22660–22669.
138 J. Mark, W. Zhang, K. Maeda, T. Yamamoto, H. Kageyama and T. Mori, *J. Mater. Chem. A*, 2023, **11**, 10213–10221.